Adaptive Piezoelectric Energy Harvesting Circuit for Wireless Remote Power Supply

Geffrey K. Ottman, *Member, IEEE*, Heath F. Hofmann, *Member, IEEE*, Archin C. Bhatt, and George A. Lesieutre

***Abstract*—This paper describes an approach to harvesting electrical energy from a mechanically excited piezoelectric element. A vibrating piezoelectric device differs from a typical electrical power source in that it has a capacitive rather than inductive source impedance, and may be driven by mechanical vibrations of varying amplitude. An analytical expression for the optimal power flow from a rectified piezoelectric device is derived, and an "energy harvesting" circuit is proposed which can achieve this optimal power flow. The harvesting circuit consists of an ac–dc rectifier with an output capacitor, an electrochemical battery, and a switch-mode dc–dc converter that controls the energy flow into the battery. An adaptive control technique for the dc–dc converter is used to continuously implement the optimal power transfer theory and maximize the power stored by the battery. Experimental results reveal that use of the adaptive dc–dc converter increases power transfer by over 400% as compared to when the dc–dc converter is not used.**

***Index Terms*—Adaptive control, dc–dc conversion, energy harvesting, low power, piezoelectric.**

I. Introduction

THE need for a wireless electrical power supply has spurred an interest in piezoelectric energy harvesting, or the extraction of electrical energy using a vibrating piezoelectric device. Examples of applications that would benefit from such a supply are a capacitively tuned vibration absorber [1], a foot-powered radio "tag" [2], [3], and a PicoRadio [4]. A vibrating piezoelectric device differs from a typical electrical power source in that its internal impedance is capacitive rather than inductive in nature, and that it may be driven by mechanical vibrations of varying amplitude and frequency. While there have been previous approaches to harvesting energy generated by a piezoelectric device [2], [3], [5], [6] there has not been an attempt to develop an adaptive circuit that maximizes power transfer from the piezoelectric device. The objective of the research described herein was to develop an approach that maximizes the power transferred from a vibrating piezoelectric transducer to an electrochemical battery. The paper initially presents a simple model of a piezoelectric transducer. An ac–dc rectifier is added and the model is used to determine the point of optimal power flow for the piezoelectric element. The paper then introduces an adaptive approach to achieving the optimal power flow through the use of a switch-mode dc–dc converter. This approach is similar to the so-called maximum power point trackers used to maximize power from solar cells [7]–[10]. Finally, the paper presents experimental results that validate the technique.

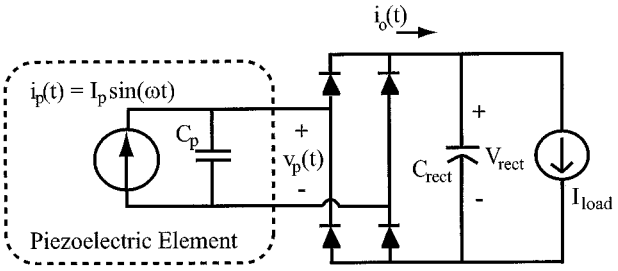

Fig. 1. Piezoelectric element model with ac–dc rectifier and load.

II. Optimal Power Flow of Piezoelectric Device

To determine its power flow characteristics, a vibrating piezoelectric element is modeled as a sinusoidal current source $i_p(t)$ in parallel with its internal electrode capacitance C_p. This model will be validated in a later section. The magnitude of the polarization current I_p varies with the mechanical excitation level of the piezoelectric element, but is assumed to be relatively constant regardless of external loading. A vibrating piezoelectric device generates an ac voltage while electrochemical batteries require a dc voltage, hence the first stage needed in an energy harvesting circuit is an ac–dc rectifier connected to the output of the piezoelectric device, as shown in Fig. 1. In the following analysis, the dc filter capacitor C_{rect} is assumed to be large enough so that the output voltage V_{rect} is essentially constant; the load is modeled as a constant current source $I_{\rm load}$; and the diodes are assumed to exhibit ideal behavior.

The voltage and current waveforms associated with the circuit are shown in Fig. 2. These waveforms can be divided into two intervals. In interval 1, denoted as u, the polarization current is charging the electrode capacitance of the piezoelectric element. During this time, all diodes are reverse-biased and no current flows to the output. This condition continues until the magnitude

Manuscript received August 27, 2001; revised May 9, 2002. Recommended by Associate Editor J. D. van Wyk. This paper was presented at the 42nd AIAA/ASME/ASCE/AHS/ASC Structures, Structural Dynamics, and Materials Conference and Exhibit, Adaptive Structures Forum, Seattle, WA, April 16–19, 2001. This work was supported by the Pennsylvania State University, Office of Naval Research, under Contract N00014–99-1–0450 and under a Subcontract from the University of Florida.

G. K. Ottman is with the Applied Physics Laboratory, Johns Hopkins University, Laurel, MD 20723 USA.

H. F. Hofmann is with the Department of Electrical Engineering, Pennsylvania State University, University Park, PA 16802 USA (e-mail: hofmann@engr.psu.edu).

A. C. Bhatt is with the Systems Design Engineering Department, Intel Corporation, Santa Clara, CA 95054 USA.

G. A. Lesieutre is with the Department of Aerospace Engineering, Pennsylvania State University, University Park, PA 16802 USA.

Publisher Item Identifier 10.1109/TPEL.2002.802194.

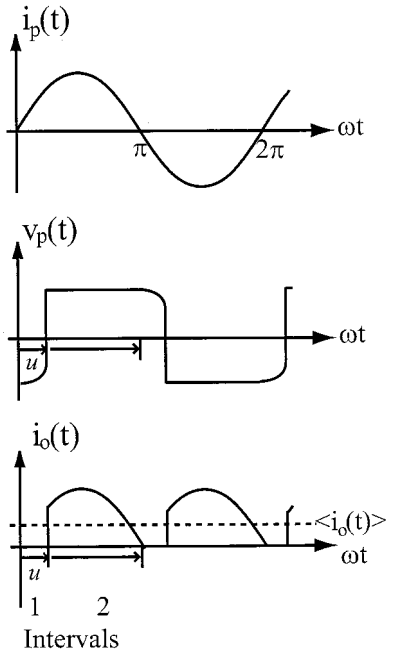

Fig. 2. Voltage, current waveforms of piezoelectric element-rectifier circuit.

of the piezoelectric voltage $v_p(t)$ is equal to the output voltage V_{rect}. At the end of the commutation interval, interval 2 begins, and output current flows to the capacitor C_{rect} and the load

$$i_o(t) = \begin{cases} 0, & 0 \le \omega t \le u \\ \frac{C_{rect}}{C_{rect}+C_p} I_p \left|\sin(\omega t)\right|, & u \le \omega t \le \pi \end{cases}. \quad (1)$$

By assuming $C_{rect} \gg C_p$, the majority of the current will be delivered as output current

$$\frac{C_{rect}}{C_{rect}+C_p} I_p \approx I_p. \quad (2)$$

The dc component of $i_o(t)$ can then be shown to be

$$\langle i_o(t) \rangle = \frac{2I_p}{\pi} - \frac{2V_{rect}\omega C_p}{\pi}. \quad (3)$$

The output power can be shown to vary with the value of the output voltage V_{rect} as follows:

$$\langle P(t) \rangle = \frac{2V_{rect}}{\pi}\left(I_p - V_{rect}\omega C_p\right). \quad (4)$$

It can then be shown that the peak output power occurs when

$$V_{rect} = \frac{I_p}{2\omega C_p} \quad (5)$$

or one-half the peak open-circuit voltage of the piezoelectric element (see Appendix for complete analysis).

III. Energy Harvesting Circuitry

The magnitude of the polarization current I_p generated by the piezoelectric transducer, and hence the optimal rectifier voltage, may not be constant as it depends upon the vibration level exciting the piezoelectric element. This creates the need for flexibility in the circuit, *i.e.*, the ability to adjust the output voltage of the rectifier to achieve maximum power transfer. To facilitate the attainment of the optimal voltage at the output of the rectifier, a dc–dc converter is placed between the rectifier output and the battery as shown in Fig. 3. Typically the controller of such a converter is designed to regulate the output voltage [11]; however, in this circuit the converter will be operated to maximize power flow into the battery. If effective, the piezoelectric element would be at peak power, which corresponds to the output voltage of the rectifier V_{rect} being maintained at its optimal value, approximately one-half the open-circuit voltage, as described previously.

The purpose of this circuit is to maximize the power flowing into the battery. As the battery voltage is essentially constant or changes very slowly, this is equivalent to maximizing the current into the battery, I_{battery}. By sensing this current, the duty cycle can be adjusted to maximize it. A control scheme such as this is general enough to be effective for many dc–dc converter topologies. To illustrate the theoretical principles of maximum power transfer and the control of the converter, a step-down or buck converter will be discussed in this paper. Fig. 4 shows a representation of the steady-state battery current – duty cycle relationship using a step-down converter.

In order to achieve peak battery current, an appropriate method of controlling the duty cycle is to incrementally increase or decrease the duty cycle as determined by the slope of the battery current curve, $\partial I/\partial D$. The duty cycle is now the sum of the present duty cycle and the increment

$$D_{i+1} = D_i + K\,\text{sgn}\left(\frac{\partial I}{\partial D}\right). \quad (6)$$

Where K is the assigned rate of change of the duty cycle and $\text{sgn}()$ is the signum function which returns the sign of the quotient $\partial I/\partial D$.

Note a few features of this control: First, as the control algorithm is based upon the sign of a rate of change, the duty cycle must continuously change in practice. Ideally, once the controller has settled, this will amount to small perturbations about the optimal operating point. Furthermore, as the control algorithm is based upon steady-state behavior of the piezoelectric element and the dc–dc converter, a two-time-scale approach must be used when designing the controller [12]. Using two-time-scale analysis techniques, convergence of the controller can be assured provided the dynamics of the control algorithm are set to be "slow" enough such that the piezoelectric device and converter can be assumed to always be operating under steady-state conditions. However, this also places limitations on the bandwidth of the controller.

IV. Control Implementation

The adaptive controller is implemented using a dSPACE DS1102 controller board. The board includes a Texas Instruments TMS320C31 floating-point digital signal processor

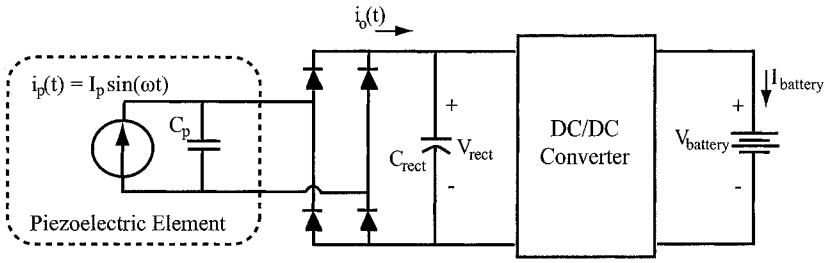

Fig. 3. Adaptive energy harvesting circuit.

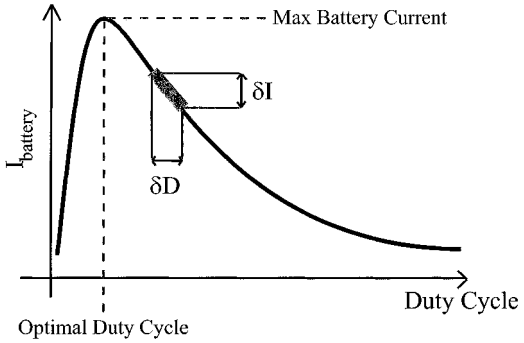

Fig. 4. Steady-state battery current as function of duty cycle, energy harvesting circuit with step-down converter.

(DSP), analog-to-digital (ADC) converters for sampling measurements, and pulse-width modulated (PWM) signal outputs for controlling the converter. The control algorithm was developed in MATLAB 5.3 using the graphical interface Simulink 3.0 and the Real-Time Workshop to generate the controller code for the DSP.

Fig. 5 shows a block diagram of the controller implementation. The initial duty cycle is set at 10% for circuit startup. The resulting battery current is evaluated using a current-sense resistor in series with the battery and sampled by an A/D converter. The current signal is then low-pass filtered to attenuate noise and reduce the current ripple effect caused by the switching of the MOSFET. The derivative of the signal is then taken and divided by the derivative of the duty cycle. Dividing the derivative of the current by the derivative of duty cycle provides $\partial I/\partial D$, which is used to determine the controller's position on the battery current–duty cycle curve shown in Fig. 4.

The sign of the quotient, $\partial I/\partial D$, is used by a 0-threshold block to increment the duty cycle by a set rate, in our case 21 millipercent/s (21-m%/s). This rate was determined to produce a measurable change in battery current that could be used to evaluate the effectiveness of the new duty cycle. The resulting sign $(+/-)$ of the division block, not its numerical magnitude, is all that is used by the 0-threshold block to increase or decrease the duty cycle. If either input signal would be zero, resulting in a zero or undefined quotient, the threshold block will decrease the duty cycle as a default. This default decrease allows the control to migrate to lower duty cycle values when the battery current might not be measurably changing, as is the case of circuit startup. Experimentation showed that, at a switching frequency of 1 kHz, the current changes little at duty cycles above 10%, whereas optimal duty cycles occurred around 3–5%.

The duty cycle is then filtered and used to generate the PWM signal for the driver circuitry of the step-down converter. The additional filtering of the PWM signal is necessary to slow the rate of change of the duty cycle so the change in current can be measured and evaluated. Without the LPF, the controller is prone to duty cycle oscillations, as the perturbing signal reacts faster than the finite settling time of the battery current signal.

V. Experimental Setup

A Quickpack® QP20W purchased from Active Control eXperts (ACX), Cambridge, MA, was used as the piezoelectric energy source. It is a two-layer device that generates an ac voltage when vibrated in a direction perpendicular to its mid-plane. Device specifications and diagram are shown in Fig. 6 along with the piezoelectric element properties.

The experimental setup is shown in Fig. 7. The piezoelectric device is secured to an electric-powered shaker, which provides variable mechanical excitation in response to a sine wave input. The magnitude of the mechanical excitation of the piezoelectric element will be characterized by the open-circuit voltage that is measured across the unloaded rectifier capacitor, V_{oc}. A small mass was added to the free tip of the bimorph to enhance the external stress and increase the tip deflection, thus providing a larger open-circuit voltage.

The step-down converter consists of a MOSFET switch with a high breakdown voltage rating, a custom wound inductor with inductance of 10.03 mH, a Schottky diode, and a filter capacitor. The voltage across the current-sense resistor is amplified with a precision op-amp (powered by the 3 V battery), and then sampled by the A/D converter on the controller card. The controller card then generates the PWM signal at the calculated duty cycle that is fed to a high-side MOSFET driver. The driver was powered by an external dc power supply. Due to the low power levels expected from the piezoelectric element [2]–[4], [6], it is assumed that the converter will operate in discontinuous current conduction mode at the chosen switching frequency of 1 kHz. Such a low switching frequency was chosen because switching losses in the experimental setup comprised a significant fraction of the power flow from the element.

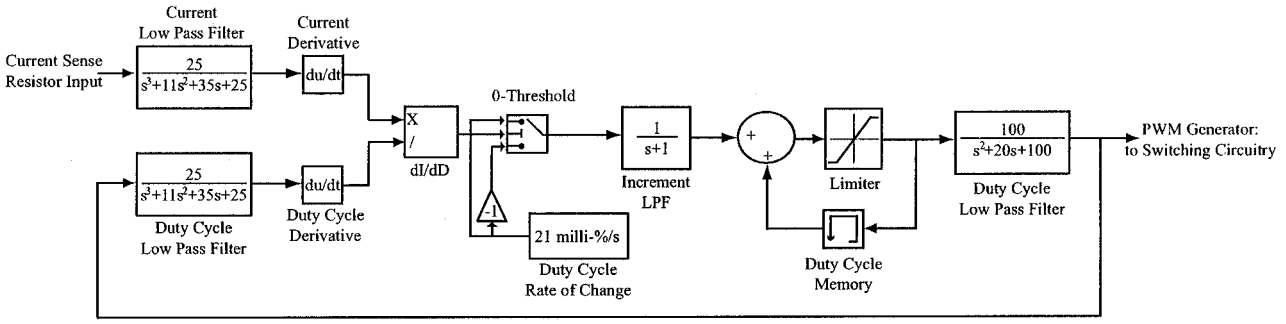

Fig. 5. Adaptive controller implementation in Simulink.

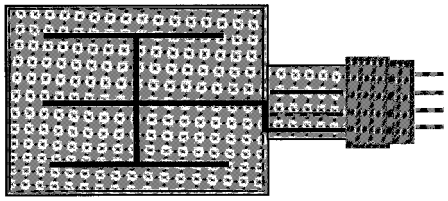

Application Type: strain actuator or bimorph actuator
Device Size (in): 2.00 x 1.50 x 0.03
Device Weight (oz): 0.28
Active Elements: 1 stack of 2 piezos
Piezo Wafer Size (in): 1.81 x 1.31 x 0.010
Device Capacitance (μF): 0.20
Full Scale Voltage Range (V): +/- 200

Property	Symbol	Units	Value
Coupling Coefficients	k_{31}		0.30
Piezoelectric Charge Coefficients (Displacement Coefficient)	d_{31}	m / V X 10^{-12} C / N X 10^{-12}	-179
Piezoelectric Voltage Coefficient (Voltage Coefficient)	g_{31}	V m / N X 10^{-3}	-11.0

Experimental Data	Symbol	Units	Value
Open-Circuit natural Vibration Freq.	ω^D	rad/s	345
Short Circuit Natural Vibration Freq.	ω^E	rad/s	330
Coupling Coefficient	k_{31}		0.29

Fig. 6. ACX model QP20W diagram and specifications, piezoelectric properties.

VI. Results

Experimental data were taken to illustrate the theories presented in this paper and to demonstrate the performance of the adaptive control algorithm. The first experiment was conducted in order to determine the validity of the piezoelectric model presented in Fig. 1. Various resistive loads were placed across the output of the excited piezoelectric element, as shown in Fig. 8, and the output voltage was measured. The frequency of excitation was adjusted to the resonant mode of the system for each resistor. This was done to ensure a relatively constant mechanical excitation level of the element throughout the experiment as the resistive load has a dampening effect on the amplitude of the mechanical vibrations. The output voltage for the circuit is given by

$$V_o = I_p \frac{R}{\sqrt{1+(\omega C_p R)^2}}. \tag{7}$$

A least squares fitting of the data to (7) resulted in I_p equal to 2.2 $\mathrm{mA_{rms}}$ and C_p equal to 0.184 μF. Substituting these values into (7), the theoretical output voltage of the circuit can be compared to the measured output voltage over a range of load resistances as shown in Fig. 9.

The next experiment was performed to validate the piezoelectric element-rectifier circuit optimal power transfer theory. Fig. 10 shows a plot of the output power versus the voltage maintained at the output rectifier for a vibrating piezoelectric element. The piezoelectric device was driven at a constant frequency of 53.8 Hz and resistors of various values were inserted across the rectifier capacitor (see Fig. 1) to provide the load. At open-circuit condition, a voltage of 45.0 V was measured across the rectifier V_{rect}. The plot of power dissipated in the resistor at various voltages shows that the maximum power of 18.0 mW is available with a 24.0 kΩ resistor at a voltage of 20.57 V. This represents the maximum dc power available for a set level of excitation and shows that maximum power occurs at a specific output voltage. The optimal rectifier voltage is close to, but slightly less than, one-half the open-circuit voltage of the piezoelectric element. A possible reason for this discrepancy is unmodeled loss mechanisms in the piezoelectric device and/or rectifier.

Using the same circuit and conditions, the output current $i_o(t)$ of the piezoelectric element was measured using a 10 Ω current-sense resistor between the rectifier and the capacitor. Fig. 11 shows the waveforms for load resistors of 430 kΩ to 0.51 kΩ across the rectifier capacitor. As the resistance is decreased, the commutation interval u becomes smaller and the current waveform is closer to a rectified sine wave.

To demonstrate that a dc–dc converter is capable of attaining the point of maximum power transfer, the step-down converter was operated with a manually varied duty cycle. Fig. 12 reveals that the battery current has a definite maximum with respect to the duty cycle. With a 45.0 V open-circuit voltage, the maximum current of 4.3 mA was measured at a duty cycle of 3.18%. At this point, the voltage at the rectifier bus capacitor was measured at 20.4 V (2 V below one-half the open-circuit voltage). The current remained above 4 mA for duty cycles between 2.5 and 4.5% and quickly decreased outside this range. The power stored by the 3 V battery was 13.0 mW at the optimal duty cycle as compared to the previous experiment, which showed 18.0

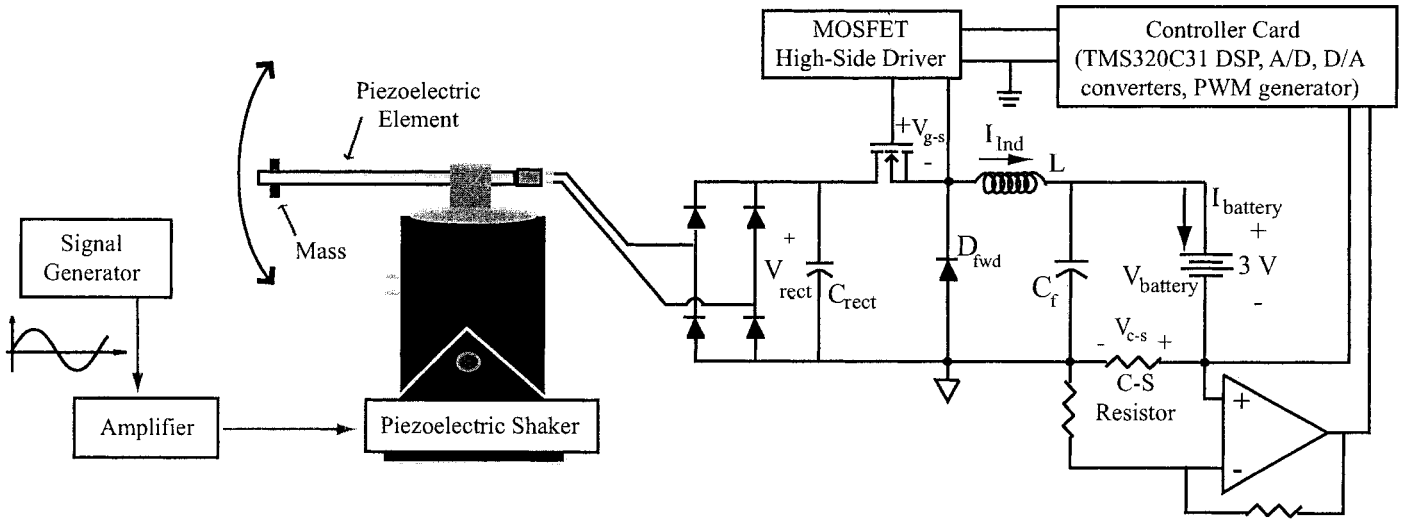

Fig. 7. Experimental circuit setup.

mW of power available with a resistive load. Power converter losses are therefore estimated to be 5 mW. For comparison, direct charging of the battery across the rectifier capacitor yielded 1.5 mA or 4.5 mW of power harvested.

The adaptive controller was then used to show that the algorithm could find and maintain the maximum power into the battery at circuit startup and adjust itself as the excitation varied. In Fig. 13, the initial duty cycle was set at 10% and the controller decreased the duty cycle linearly as the current increases. With an open-circuit voltage of 45.8 V, the controller settled to the maximum current of 4.3 mA. The controller then maintained maximum power transfer, while perturbing the duty cycle slightly.

The settling time illustrates the duty cycle rate of change, 21-m%/s, and its effects. The value allows meaningful changes to the current to be measured without large oscillations around the maximum power point. This value does limit the controller speed at startup, taking almost 6 min to achieve maximum current, but once the optimum duty cycle is determined, it limits the oscillations that would increase the time away from the optimum duty cycle. Smaller rates of change that were investigated did not allow changes in the current to be reliably measured and larger rates caused inefficient harvesting due to increased duty cycle oscillations.

Waveforms for step-down converter operation are shown in Fig. 14. Shown are the rectifier capacitor voltage V_{rect} (mean of 20.3 V), the MOSFET gate-to-source voltage $V_{\mathrm{g-s}}$, the current sense resistor voltage $V_{\mathrm{c-s}}$, and the inductor current I_{Ind}. The battery voltage, which is not shown, is constant at 3.0 V. The MOSFET rise and fall times were measured at 6.5 and 18.5 ns respectively. The controller is stabilized at an optimal duty cycle of 3.18% corresponding to 13.0 mW of harvested power. The discontinuous current conduction mode of the converter can be seen in the inductor current waveform.

The final experiment considered shows the superior performance of the adaptively controlled step-down converter for harvesting energy. Direct charging of the 3 V battery (the battery connected across the rectifier capacitor) is a simple, nonadaptive approach to energy harvesting that was sought to be improved upon. By comparing these two methods with the

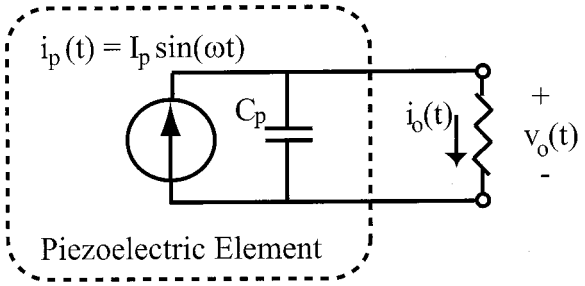

Fig. 8. Piezoelectric element model with resistive load.

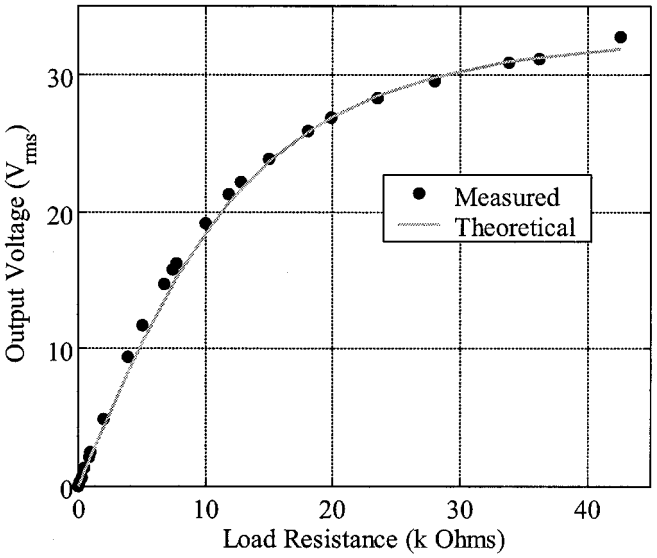

Fig. 9. Output voltage of piezoelectric element with resistive load ($V_{oc} = 35.8 V_{rms}$).

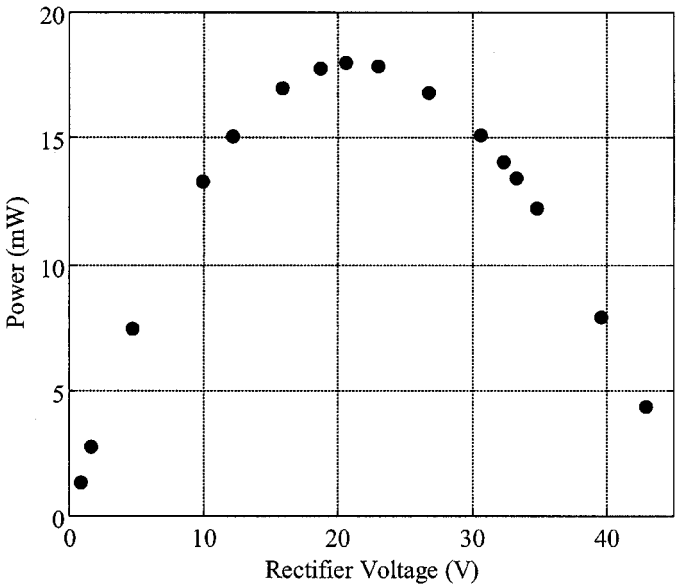

Fig. 10. Output power versus rectifier voltage ($V_{oc} = 45.0V$).

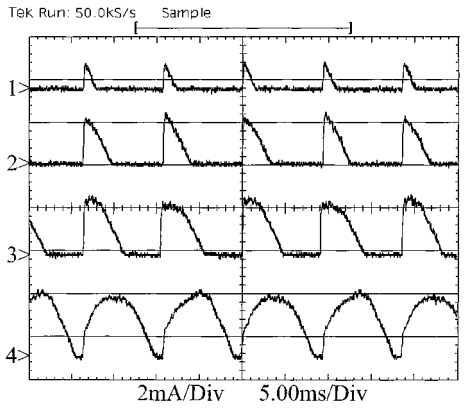

Fig. 11. Piezoelectric element output current $i_o(t)$ with resistive loading $V_{oc} = 45.0V$.

1) $R_{load} = 430k\Omega < i_o(t) >= 0.040mA\ V_{rect} = 42.90V$
2) $R_{load} = 75k\Omega < i_o(t) >= 0.347mA\ V_{rect} = 32.32V$
3) $R_{load} = 24k\Omega < i_o(t) >= 0.791mA\ V_{rect} = 20.57V$
4) $R_{load} = 0.51k\Omega < i_o(t) >= 1.828mA\ V_{rect} = 0.82V$

maximum available power (the power measured with the optimal resistance across the rectifier capacitor), the advantages of the controller can be clearly seen. The piezoelectric element was adjusted to its resonance frequency for each specific load or for the converter operating condition and the power flow results for various excitation levels are shown in Fig. 15. At the highest excitation level considered, the rectified open-circuit voltage was measured at 95.31 V. At this level, the harvested power increased from 16.43 mW without the step-down converter to 70.42 mW with the step-down converter, over a factor of 4 improvement. The plot clearly shows the step-down converter outperforming the direct charging of the 3 V battery at all levels of excitation. The converter follows the same general curve as the maximum available power, increasing with the square of the voltage, and shows that as the piezoelectric element is driven harder; the converter becomes more and more essential for effective harvesting. The controller resulted in the rectifier voltage consistently at 42% of the open-circuit voltage, which is reasonably close to the predicted one-half. Based on the power level of a single piezoelectric element, it is anticipated that an extensive array of piezoelectric material would be necessary to make an adaptive controller of this type feasible if the control circuitry is to be powered from the mechanical vibrations.

An estimate of converter losses can be calculated as the difference between the maximum and harvested power. The efficiency of the rectifier is not considered. The efficiency of the step-down converter was between 74 and 88% with the efficiency decreasing as the excitation was increased. At the highest excitation the losses were 18.87 mW. Because efficiency of the step-down converter suffers when the output voltage is significantly less than the input voltage, other dc-dc converter topologies may be more suitable for applications where high mechanical excitation of the piezoelectric element is expected.

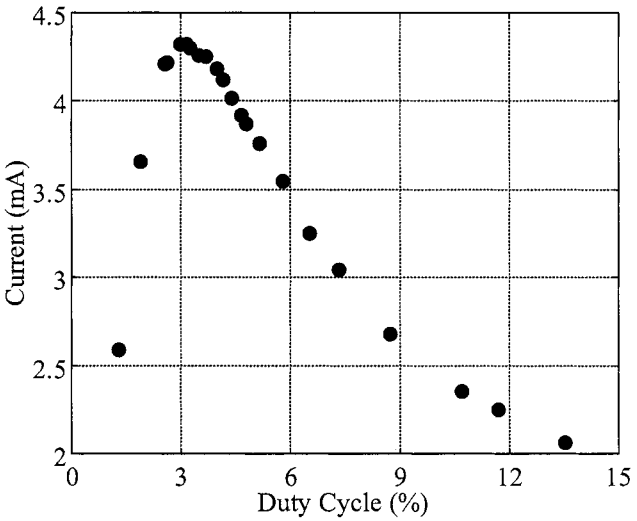

Fig. 12. Battery current versus duty cycle ($V_{oc} = 45.0V$).

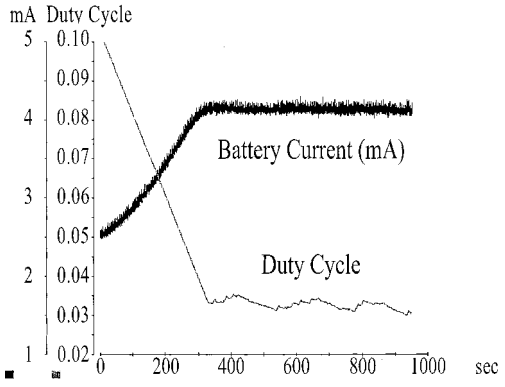

Fig. 13. Adaptive controller at startup.

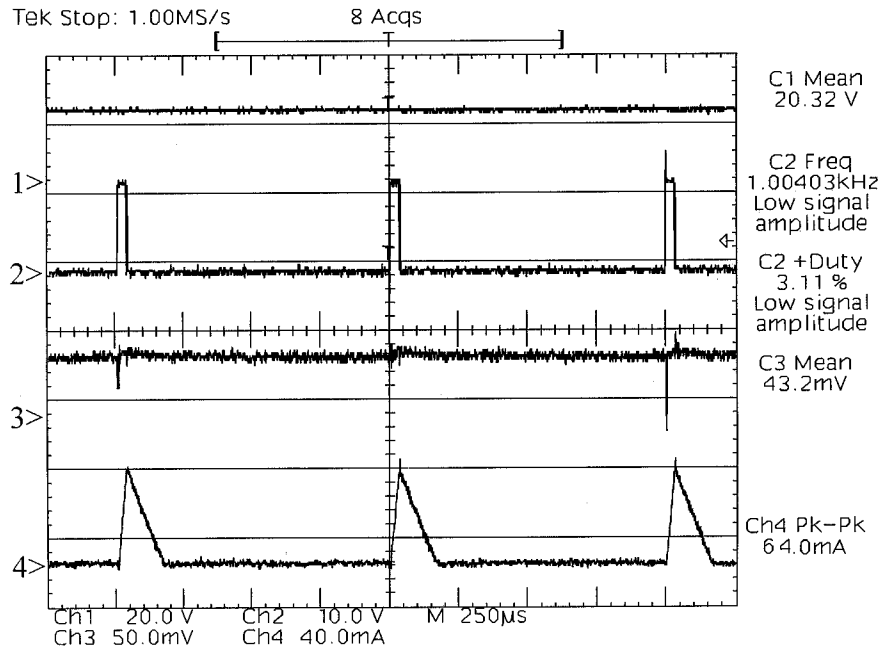

Fig. 14. Step-down converter voltage waveforms ($V_{oc} = 45.0V$): $V_{rect}, V_{g-s}, V_{c-s}$, and I_{Ind}.

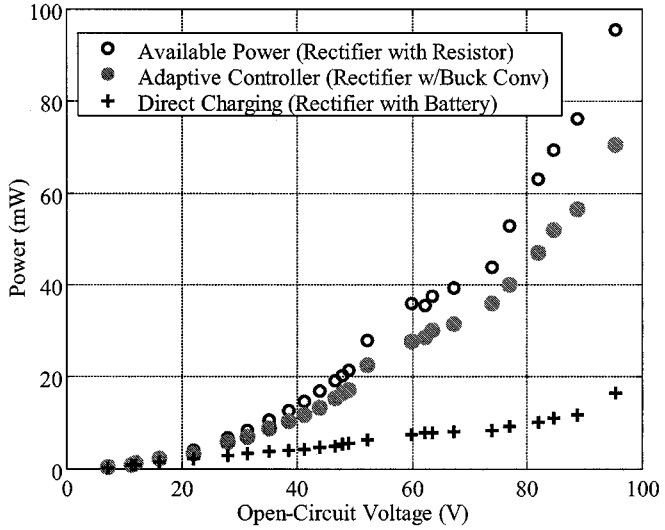

Fig. 15. Power stored by 3 V battery.

VII. Conclusions

This paper presents an adaptive approach to harvesting electrical energy from a mechanically excited piezoelectric element. The dc–dc converter with an adaptive control algorithm harvested energy at over four times the rate of direct charging without a converter. Furthermore, this rate is expected to continue to improve at higher excitation levels.

The flexibility of the controller allows the energy harvesting circuit to be used on any vibrating structure, regardless of excitation frequency, provided a piezoelectric element can be attached. Also, external parameters such as device placement, level of mechanical vibrations or type of piezoelectric devices will not affect controller operation. The control algorithm can also be applied to other dc–dc converter topologies. This would allow the development of optimized system designs based upon the expected excitation or the electronic load that is to be powered. Future work will focus on the design of an optimized system design using standalone control circuitry.

Appendix
Derivation of Output Power Equations for Rectified Piezoelectric Element

The current produced by the rectified piezoelectric element can be related to the change of the element's voltage through the device capacitance during the commutation interval

$$I_p \sin(\omega t) = C_p \frac{\partial v_p}{\partial t}. \tag{8}$$

Rewriting the right side of the equation as $\omega C_p \partial v_p / \partial(\omega t)$ and integrating this during the commutation interval $0 < \omega t \leq u$ and setting $v_p(0) = -V_{rect}$ and $v_p(u) = +V_{rect}$

$$\int_0^u I_p \sin(\omega t) \partial(\omega t) = \omega C_p \left(v_p(u) - v_p(0)\right) \tag{9}$$

$$I_p \left(-\cos(\omega t)|_0^u\right) = 2V_{rect}\omega C_p \tag{10}$$

which reduces to

$$\cos(u) = 1 - \frac{2V_{rect}\omega C_p}{I_p}. \tag{11}$$

During the commutation interval no current flows to the rectifier and the load. Once the piezoelectric element's electrode capacitance is charged to the voltage of the rectifier capacitor voltage, current flows to the load during the remainder of the half-cycle, the interval $u < \omega t \leq \pi$. During this interval, the output current can be determined by relating the internal piezoelectric element capacitance to the output capacitance

$$i_o(t) = \frac{C_{rect}}{C_{rect} + C_p} i_p(t). \tag{12}$$

By assuming $C_{rect} \gg C_p$

$$i_o(t) = i_p(t). \tag{13}$$

Solving for the average value of the load current during half of the sine wave, the interval $0 < \omega t \leq \pi$

$$\langle i_o(t) \rangle = \frac{1}{\pi} \left(0 + \int_u^{\pi} I_p \sin(\omega t) \partial(\omega t) \right) \tag{14}$$

$$\langle i_o(t) \rangle = \frac{I_p}{\pi} (1 + \cos(u)). \tag{15}$$

Inserting (11) results in an expression for load current

$$\langle i_o(t) \rangle = \frac{2I_p}{\pi} - \frac{2V_{rect}\omega C_p}{\pi}. \tag{16}$$

The average value of the output voltage is

$$\langle v_o(t) \rangle = V_{rect}. \tag{17}$$

The average output power of the piezoelectric element can now be calculated as the product of (16) and (17)

$$\langle P(t) \rangle = \frac{2V_{rect}}{\pi} (I_p - V_{rect}\omega C_p). \tag{18}$$

REFERENCES

[1] C. Davis and G. Lesieutre, "An actively tuned solid-state vibration absorber using capacitive shunting of piezoelectric stiffness," *J. Sound Vibration*, vol. 232, no. 3, pp. 601–17, May 2000.

[2] J. Kymissis, C. Kendall, J. Paradiso, and N. Gerhenfeld, "Parasitic power harvesting in shoes," in *Proc. 2nd Int. Symp. Wearable Comput.*, Pittsburgh, PA, Oct. 19–20, 1998, pp. 132–139.

[3] N. Shenck and J. A. Paradiso, "Energy scavenging with shoe-mounted piezoelectrics," *IEEE Micro*, vol. 21, pp. 30–42, May-June 2001.

[4] J. M. Rabaey, M. J. Ammer, J. L. da Silva Jr, D. Patel, and S. Roundy, "PicoRadio supports ad hoc ultra-low power wireless networking," *Comput.*, vol. 33, no. 7, pp. 42–48, July 2000.

[5] P. Smalser, "Power transfer of piezoelectric generated energy," U.S. Patent, 5 703 474, 1997.

[6] P. Glynne-Jones, S. P. Beeby, and N. M. White, "Toward a piezoelectric vibration-powered microgenerator," *Proc. IEEE*, vol. 148, pp. 68–72, Mar. 2001.

[7] J. H. R. Enslin and D. B. Snyman, "Simplified feed-forward control of the maximum power point in PV installations," in *Proc. 1992 Int. Conf. Ind. Electron., Contr., Instrum., Automat.*, vol. 1, San Diego, CA, Nov. 9–13, 1992, pp. 548–553.

[8] C. R. Sullivan and M. J. Powers, "A high-efficiency maximum power point tracker for photovoltaic arrays in a solar-powered race vehicle," in *Proc. 24th Annu. IEEE Power Electron. Spec. Conf.*, Seattle, WA, June 20–24, 1993, pp. 574–580.

[9] C. Hua and C. Shen, "Study of maximum power tracking techniques and control of dc/dc converters for photovoltaic power system," in *Proc. 29th Annu. IEEE Power Electron. Spec. Conf.*, vol. 1, Fukuoka, Japan, May 17–22, 1998, pp. 86–93.

[10] E. Koutroulis, K. Kalaitzakis, and N. Voulgaris, "Development of a microcontroller-based photovoltaic maximum power point tracking control system," *IEEE Trans. Power Electron.*, vol. 16, pp. 46–54, Jan. 2001.

[11] N. Mohan, T. Undeland, and W. Robbins, *Power Electronics: Converters, Applications and Design*. New York: Wiley, 1995.

[12] P. Kokotovic, H. Khalil, and J. O'Reilly, *Singular Perturbation Methods in Control: Analysis and Design*. New York: Academic, 1987.

Geffrey K. Ottman (M'02) received the B.S. degree in electrical engineering from the U.S. Coast Guard Academy, New London, CT, in 1995 and the M.S. degree in electrical engineering from the Pennsylvania State University, University Park, in 2002.

He is currently with the Applied Physics Laboratory, Space Systems Department, Johns Hopkins University, Laurel, MD. His research interests include power electronics and converter design.

Heath F. Hofmann (M'90) received the B.S. degree in electrical engineering from the University of Texas, Austin, in 1992, and the M.S. and Ph.D. degrees in electrical engineering from the University of California, Berkeley, in 1997 and 1998, respectively.

He began his career at The Pennsylvania State University, University Park, as an Assistant Professor in the Department of Electrical Engineering. His research interests are in power electronics and electromechanical systems. He is the primary coauthor on several journal papers on electric machine design and control. Specific interests are the development and application of sensorless field-oriented control schemes, quiet electric drives, high-speed machine design, piezoelectric power generation, and the application of advanced numerical methods to the design and simulation of electromechanical systems, focusing on finite-element analysis techniques.

Dr. Hofmann received the Prize Paper Award from the Electric Machines Committee, IEEE IAS Annual Meeting, in 1998.

Archin C. Bhatt received the M.S. degree in electrical engineering from the Pennsylvania State University, University Park, in 2000.

He is currently with Intel, Santa Rosa, CA, where he is responsible for designing high–speed systems/subsystems, including memory and interconnects. He is also responsible for electrical simulation of high–speed interconnects on motherboards.

George A. Lesieutre received the B.S. degree in aeronautics and astronautics from the Massachusetts Institute of Technology, Cambridge, in 1981, and the Ph.D. degree in aerospace engineering from the University of California, Los Angeles, in 1989.

From 1977 to 1989, he held positions at Argonne National Laboratory, Allison Gas Turbines, Rockwell International Satellite Systems Division, and SPARTA. In 1989, he joined the faculty of the Department of Aerospace Engineering, Pennsylvania State University, University Park. His research interests include the dynamics of adaptive aerospace vehicles and composite structures; vibration control, with emphasis on passive damping; piezoelectric actuators; and tunable transducers.

Dr. Lesieutre received best paper awards from the American Institute of Aeronautics and Astronautics (AIAA), the American Society of Mechanical Engineers, and the American Helicopter Society. He is an Associate Fellow of the AIAA, which he presently serves as Chair of the Adaptive Structures Technical Committee.